Volume 59, Issue 5, March 2011   ISSN 1359-6454

ELSEVIER

Acta MATERIALIA

STRUCTURE   PROPERTIES

THEORY   PROCESSING

FUNCTION

⟨110⟩

2 mm

0°   28°

Available online at ScienceDirect www.sciencedirect.com   www.elsevier.com/locate/actamat

Thermo-physical properties of thin films composed of anatase TiO$_2$ nanofibers

X. Feng, X. Wang*, X. Chen, Y. Yue

Department of Mechanical Engineering, 2010 Black Engineering Building, Iowa State University, Ames, IA 50011, USA

Abstract

In this paper, anatase titanium dioxide (TiO$_2$) thin films ∼60 μm thick are fabricated using the electrospinning technique. The prepared thin films are composed of interconnected anatase TiO$_2$ nanofibers. The transient electro-thermal technique, combined with a temperature–resistance calibration procedure, provides a full spectrum study which examines the relationship between the film's thermal diffusivity, density and thermal conductivity. It is found that the annealing process significantly reduces the thermal diffusivity of the sample from 3.73×10^{-5} m^2 s^{-1} to the order of 10^{-6} m^2 s^{-1}. The effective thermal diffusivity, conductivity and density of the films are 1.35–3.52×10^{-6} m^2 s^{-1}, 0.06–0.36 W m^{-1} K^{-1} and 25.8–373 kg m^{-3}, respectively. These values are about one order of magnitude or more lower than the bulk property values. This difference is attributed to the loose interior structure and large concentration of vacancies. A microscale physical model is designed to explore the intrinsic thermal conductivity of the discrete TiO$_2$ nanofibers that compose the films. The calculated intrinsic thermal conductivity of the TiO$_2$ nanofibers varies from 4.67 to 12.2 W m^{-1} K^{-1}, which is comparable with the bulk thermal conductivity of 8.5 W m^{-1} K^{-1}. The phonon mean free path calculation demonstrates that the nanofiber size has a negligible impact on the phonon transport. The major restriction on the heat transfer originates from the crystalline structure defect.
© 2010 Acta Materialia Inc. Published by Elsevier Ltd. All rights reserved.

Keywords: Thin films; Anatase TiO$_2$; Transient electro-thermal; Thermal conductivity

1. Introduction

TiO$_2$ is a promising inorganic functional material and has received tremendous attention for decades. This is because of its novel applications in electronics, photocatalysts, dye-sensitized solar cells, photolysis of water, and many other areas. The unique properties of TiO$_2$ are significantly influenced by its crystal morphology, particle size, surface area and porosity. With the development of nanotechnology, the synthesis of nanoscale TiO$_2$ material and the measurement of the electrical and thermal properties have attracted rapidly increasing exploration, and numerous related achievements have been reported. The sol–gel technique [1–3], chemical vapor deposition (CVD) [4–6],

electrospinning technique [7–13] and many other techniques have been extensively employed for preparing TiO$_2$ nanofibers [7–13], nanopowders [14], nanotubes [15,16], nanowires [17–21] and thin films [4–6,22–29]. Among all nanophases, TiO$_2$ thin film, which is fabricated via various methods [4–6,22–29], is substantially important in several applications, such as protective coatings, microelectronic applications, optical coatings and photochemically active layers. The research on the physical properties of TiO$_2$ thin films has been carried out focusing on diverse aspects. The electrical conductivity of TiO$_2$ thin films was studied by Gu et al. [30] to explore the effect of film thickness and substrate material on which the film is deposited by magnetron sputtering. For thermal properties, Zhang et al. [31] investigated the thermal diffusivity of nanostructured TiO$_2$ thin films on silicon substrate and concluded that the thermal diffusivity is also dependent on film thickness and annealing temperature. Moreover,

* Corresponding author. Tel.: +1 515 294 2085; fax: +1 515 294 3261.
E-mail address: xwang3@iastate.edu (X. Wang).

plenty of findings have been reported on thermal conductivity, which is the key property in determining the capability of TiO_2 to transfer heat. A direct reading thermal comparator [32] was used to measure the thermal conductivity of TiO_2 thin film coatings, and it was found that the thermal conductivity is several orders of magnitude lower than that of bulk material. For electron-beam (EB) deposited and ion-plated (IP) thin films of TiO_2, Wu et al. [33] studied both absorption and thermal conductivity. The films fabricated by EB and IP techniques both show much lower thermal conductivity than bulk material, while IP coatings presented higher thermal conductivity than EB coatings. Cahill and Allen [34] also measured the thermal conductivity of TiO_2 optical coatings fabricated by reactive evaporation and ion beam sputtering. The results indicated a thermal conductivity of $\sim$6–16 mW cm^{-1} K^{-1}, which is lower than the reported value for bulk TiO_2. The 3ω method was adopted by Lee et al. [35] to measure the thermal conductivity of rutile-structured microcrystalline TiO_2 film. A strong dependence of thermal conductivity on substrate temperature was observed. When the substrate temperature is $\sim$400 °C, the thermal conductivity approaches the bulk thermal conductivity of $\sim$8 W m^{-1} K^{-1}. The in-plane thermal conductivity of TiO_2 thin film [36] was measured using the thermo-reflectance method, and the results indicated that the thermal conductivity is one order of magnitude smaller than the bulk property value. TiO_2 films of different phases including crystalline, non-crystalline and amorphous were all measured by Martan et al. [37] using a two-detector measurement system of pulse photothermal radiometry. The measurement revealed that anatase has a higher thermal conductivity than the rutile and amorphous phases. Maekawa et al. [5] investigated the TiO_2 films grown by metal organic CVD and the relationship between the microstructure and thermal conductivity, which showed that the feather-like texture film exhibited a much lower thermal conductivity than the bulk TiO_2.

Though experiments have been undertaken to study the thermo-physical properties of TiO_2 films, most of them have concentrated on the films fabricated directly on substrates by the sputtering method or vapor deposition technique. Other than thin films deposited on substrates, little work has been reported regarding the thermo-physical properties of discrete TiO_2 thin films consisting of interconnected networks of nanofibers. The transient electro-thermal (TET) technique has been developed as an effective transient method of measuring the thermo-physical properties of various materials. The validity of the technique for measuring the thermal diffusivity of conductive, semi-conductive and non-conductive materials was confirmed by Guo et al. [38] in the present authors' laboratory. The results were close to literature values with <10% deviation, demonstrating the capability and accuracy of the TET technique in measuring thermal diffusivity. In addition, the thermal conductivity and specific heat of individual thin platinum wires were also measured simultaneously using the TET technique in Feng et al.'s work [39]. The

experimental results gave good conformity with literature values. For TiO_2 materials, Guo et al. [40] applied the TET technique to explore the anisotropic thermal conductivity of highly ordered amorphous and anatase TiO_2 nanotube arrays. Many publications have shown that the TET technique can measure thermo-physical properties with a strong signal level, much reduced measurement time and relatively high accuracy.

In this paper, the TET technique is applied to investigate the thermo-physical properties of discrete TiO_2 thin films composed of interconnected nanofibers. In Section 2, the sample preparation procedure is introduced, and auxiliary devices are adopted to examine the nanostructure of prepared samples. Then the TET technique is used with the samples to characterize their thermo-physical properties. In Section 3, the fitting result of a selected sample is presented to demonstrate the measurement capacity of the fast TET technique in measuring the TiO_2 material. Furthermore, thermal diffusivity, thermal conductivity and density of all samples are presented to analyze the connection between the physical and thermal properties. A simplified physical model is developed to investigate the intrinsic thermal conductivity of the TiO_2 nanofibers that compose the thin films.

2. Experimental procedure

2.1. Sample preparation

The electrospinning method [7,10] is employed for preparing a fibular mesostructure composed of nanofibers, and its experimental setup can be seen in Fig. 1. In this procedure, 1.5 g of titanium tetraisopropoxide (Ti(OiPr)$_4$) is mixed with 3 mL of acetic acid and 3 mL of ethanol. After 10 min, the solution is mixed with another 7.5 mL of ethanol containing 0.45 g of PVP (Aldrich; $M_w \approx 1300,000$), followed by magnetic stirring for $\sim$1 h in a capped vial. The well-stirred solution is immediately loaded into a
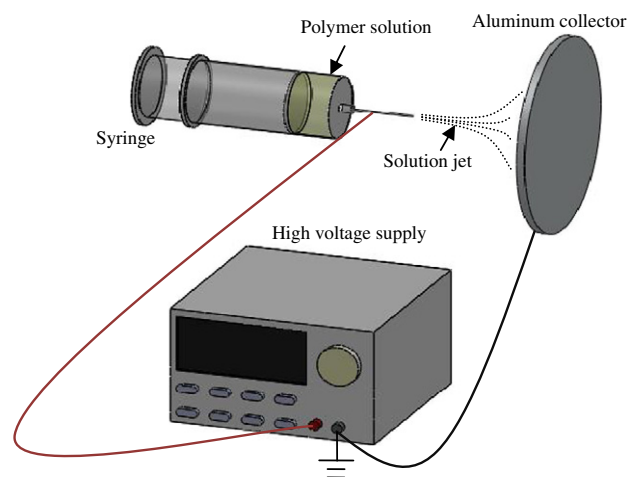
Fig. 1. Schematic illustration of the experimental setup for the electrospinning technique.

syringe equipped with a 23-gauge stainless-steel needle. The needle is connected to a 20 kV ultra-high-voltage source which is supplied by a power supply and a voltage amplifier which is able to amplify an input voltage by 1000 times. A plate wrapped with aluminum foil is placed 6 cm below the needle tip for collecting purposes. The entire electrospinning process is performed in open air. With the ultra-high electric field around $3.3\ kV\ cm^{-1}$, the polymer solution in the syringe is injected from the needle and is stretched into continuous ultrathin fibers. Given a certain duration time, the fibers collected by the aluminum foil form a thin film, which actually consists of numerous discrete nanofibers.

The as-spun film is left in open air for ∼5 h to allow the continued hydrolysis of $Ti(OiPr)_4$ to finish, and then the PVP compound is selectively removed from the film by annealing in open air at 500 °C for 3 h. Atomic force microscopy (AFM) is employed to study the surface topography of the samples both before and after annealing, and the images are presented in Fig. 2. As observed in these images, each individual nanofiber has an approximately uniform cross-sectional area, and the average diameter is in the range 300–1050 nm (left image in Fig. 2). Because $Ti(OiPr)_4$ can be rapidly hydrolyzed by moisture in the air, continuous networks (gel) of TiO_2 sols are able to keep forming nanofibers. As the PVP is selectively removed from the sample using annealing, the nanofibers maintain the continuous structures, while the average diameter decreases to ∼200–700 nm (right image in Fig. 2). This size reduction could be explained by the evaporation of PVP from the nanofibers and also the crystallization of TiO_2.

In order to identify the polymorph of the TiO_2 samples precisely, Raman spectroscopy is conducted on the samples, and the spectra of as-prepared and annealed samples are presented in Fig. 3. For the as-prepared film at room temperature, the spectra indicate no distinct peaks, but only trivial fluctuation. However, explicit Raman peaks are observed with the annealed sample. Broader features are located in the range $100–1000\ cm^{-1}$, and four distinct Raman peaks are observed at 135, 392, 515 and $633\ cm^{-1}$. This peak distribution is in perfect accordance with previous results [41,42], and the annealed sample can be identified as an anatase polymorph of TiO_2. The Raman peak at $135\ cm^{-1}$ is very sharp, and it has been identified as a symbolic peak for anatase crystal structure when compared with rutile crystal, which is another typical
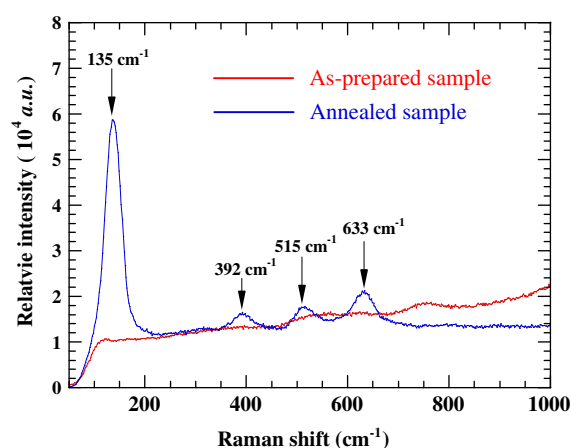
Fig. 3. Raman spectrum of TiO_2 film at room temperature and 500 °C.

polymorph of TiO_2. The rutile crystal can be transformed into anatase under higher temperature annealing. Based on the GF-matrix method using the force constants given in Ohsaka et al.'s work [41], the peaks at $135\ cm^{-1}$ and $392\ cm^{-1}$ are the O–Ti–O bending-type vibrations, and the other modes with peaks at $515\ cm^{-1}$ and $633\ cm^{-1}$ represent Ti–O bond stretching-type vibrations.

After obtaining the anatase TiO_2 thin films, another process is necessary for the samples to be measured efficiently by the TET technique. Because of the poor electrical conductivity of TiO_2 for acquiring strong signals, an ultra-thin Au film is coated on one side of the film to make it capable of quickly conducting transient electric current and thermal sensing. The coating procedure is executed using a Denton vacuum coating device and the coating process continues for 200 s, which is estimated to generate a film 100 nm thick. The following sections examine the influence of the Au coating on the measurement of thermo-physical properties.

2.2. R–T calibration

For Au-coated TiO_2 film, the electrical conductance and thermal conductance were improved significantly compared with an uncoated sample. In order to determine the temperature coefficient of resistance for the samples, a calibration procedure is conducted before the TET measurement is carried out. The Au-coated film is suspended between two
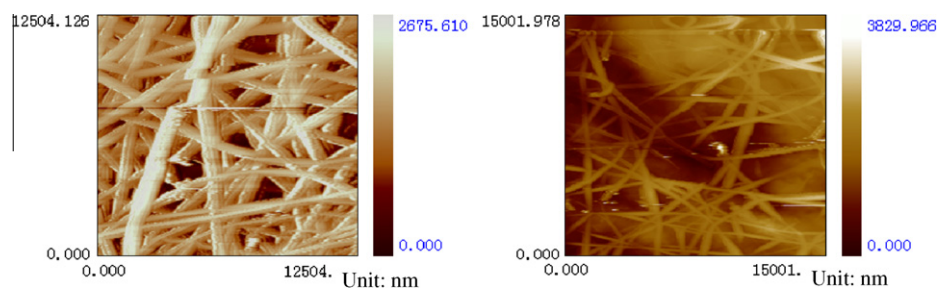
Fig. 2. AFM images of nanostructure of TiO_2 thin film: (left) before annealing; (right) after annealing.

aluminum electrodes. The bottom side of the film is in direct thermal contact with the electrodes, and silver paste is used to attach the film to the electrode to ensure optimal heat dissipation. The compression induced by the silver paste is negligible, because it does not cause planar deformation, while the induced tension is controlled to be as small as possible to avoid distinct film expansion. After the silver paste completely dries, a K-type thermocouple is attached to one side of the electrode close enough to the sample, and the other end of the thermocouple is connected to a thermocouple meter to monitor the temperature change simultaneously. The whole stage, including the aluminum electrodes and the sample suspended between the electrodes, is positioned on a heating plate. This calibration procedure is conducted in a vacuum chamber with the pressure kept $<10^{-3}$ torr to reduce unnecessary heat dissipation. Because of the fragility of the sample, moderate heating is used in calibration to ensure that the signal is strong enough and the sample remains intact. After the temperature reaches ~45 °C, the heating is turned off and the cooling process begins. During the cooling process, the temperature decrease is relatively slow compared with the heating process. Therefore, the time can be assumed to be long enough to achieve an even temperature distribution, and the readings from the thermocouple meter can be approximated as the temperature of the sample. Both temperature and resistance readings are recorded to attain the temperature-resistance calibration profile for further data processing.

2.3. TET experiment principles

The TET technique [38] has been proved a powerful approach to measuring the thermal properties of conductive, semi-conductive and even non-conductive materials. Compared with 3ω, optical heating and electrical thermal sensing techniques, the TET technique features a much stronger signal level (hundreds to thousands of times higher) and a significantly reduced measurement time (<1 s). A schematic of the TET experiment setup is shown in Fig. 4a. The TET technique is conducted with the film immediately after the temperature-resistance calibration. At the beginning of the experiment, a step DC current is fed through the sample to generate electric heat. The transient temperature increase profile of the sample is closely related to heat transfer along the length direction, since the length scale is much greater than that of the other two directions. The temperature variation along the sample induces electrical resistance change, which leads to an overall voltage change of the sample.

In this experiment, the voltage change of the sample will be monitored by an oscilloscope and a relative temperature evolution is also derived with the known voltage variation. A typical U–t profile recorded by the oscilloscope is presented in Fig. 4b. This profile contains a rising phase followed by a steady state when heat transfer equilibrium is achieved. U_0 is the initial voltage when the current begins to feed, and U_1 is the voltage at its steady state. The tran-
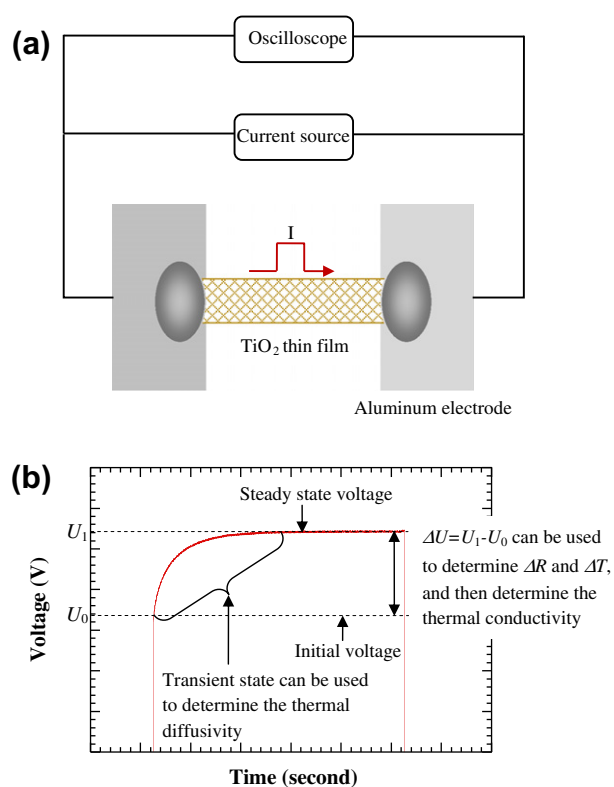
Fig. 4. (a) Schematic of the experimental principle and the step current provided for the TET technique, and (b) methodology to determine the thermo-physical properties based on the experimental U–t profile.

sient state during the rising phase is used for fitting to determine thermal diffusivity. As explained in Fig. 4b, the voltage difference ΔU is used to calculate ΔR, ΔT and thermal conductivity.

The physical model of the TET technique is developed from a one-dimensional heat conduction problem. In the whole process, electric heating q_0 is assumed constant. However, the heating power changes slightly with resistance variation in this procedure. Since the aluminum stage is much larger than the sample dimension, the temperature of both electrodes is assumed to be room temperature. Without considering the radiation effect (which is negligible for this measurement), the governing equation of this one-dimensional heat conduction problem is

$$\frac{\partial(\rho c_p T)}{\partial t} = k \frac{\partial^2 T}{\partial x^2} + q_0 \tag{1}$$

where ρ, c_p and k are density, specific heat, and thermal conductivity of the sample, respectively. The detailed procedure to solve this governing equation is given in Guo's work [38]. Only the solution is presented here for data analysis, and the average temperature of the sample $T(t)$ is calculated as

$$T(t) = \frac{1}{L} \int_{x=0}^{L} T(x,t)dx$$

$$= T_0 + \frac{8q_0 L^2}{k\pi^4} \sum_{m=1}^{\infty} \frac{1 - exp\left[-(2m-1)^2 \pi^2 \alpha t / L^2\right]}{(2m-1)^4} \tag{2}$$

When the time is long enough, the temperature distribution along the sample will reach the steady state, and the average temperature of the wire becomes $T_0 + q_0 L^2/(12k)$. q_0 is the electrical heating power per unit volume and can be expressed as $q_0 = I^2 R/(AL)$, while A and L are the cross-sectional area and length of the sample, respectively. With the calibration result of temperature coefficient of resistance η and the resistance change ΔR during the heating process, the temperature change ΔT is calculated, and then the thermal conductivity is obtained as $k = I^2 RL/(12A\Delta T)$. Meanwhile, the normalized temperature increase is written as

$$T^* = \frac{96}{\pi^4} \sum_{m=1}^{\infty} \frac{1 - exp\left[-(2m-1)^2\pi^2\alpha t/L^2\right]}{(2m-1)^4} \tag{3}$$

The voltage evolution (U_{sample}) recorded by the oscilloscope is directly related to the average temperature change of the sample as

$$U_{sample} = IR_0 + I\eta\frac{8q_0L^2}{k\pi^4} \times \sum_{m=1}^{\infty}$$
$$\frac{1 - exp\left[-(2m-1)^2\pi^2\alpha t/L^2\right]}{(2m-1)^4} \tag{4}$$

where U_{sample} is the voltage over the sample recorded by the oscilloscope, I is the constant current fed through the sample, R_0 is the resistance of the sample without heating, and η is the temperature coefficient of resistance of the sample. Therefore, it is clear that the measured voltage change is inherently related to the temperature change of the sample.

Because the film is Au-coated to avoid weak electric response, the measured effective thermal diffusivity (α_e) combines the effects of both the sample and the thin Au film. The thermal effect caused by the coated layer can be subtracted using the Lorenz number without increasing the uncertainty [38]. The thermal diffusivity (α) of the sample is calculated as

$$\alpha = \alpha_e - \frac{L_{Lorenz}TL}{RA_w\rho c_p} \tag{5}$$

where ρ and c_p are the density and specific heat of the bare film, and L_{Lorenz} is the Lorenz number. With known parameters, the modification is achievable to eliminate the effect of the Au film.

3. Results and discussion

3.1. TET measurement of thermal conductivity and thermal diffusivity

The thickness of all the prepared samples is ~60 μm, while the length and width are of millimeter scale. Compared with the length and width, whose measurement uncertainty is just ~2–3%, it is more difficult to determine the thickness precisely. This is because the fabricated films

have loose internal structures; they are not tightly condensed, as clearly demonstrated in Fig. 2. When external force is applied by the micrometer caliper, the thickness is likely to change, and it introduces a certain degree of uncertainty into the experiment. In addition, the thickness of each sample is not perfectly uniform along the planar direction. A slight fluctuation of hundreds of nanometers is observed using an atomic force microscope. Considering these factors, three measurements are performed for each sample to obtain an average value of thickness. This reduces the influence of measurement uncertainty. A consequent uncertainty is estimated to be ~10%, the effect of which is included in further discussion. A selected sample is used to present the experiment and data processing. Detailed information about the sample dimension and experimental conditions are listed in Table 1, and a microscopic image of this sample is shown in Fig. 5a, in which the length and width are marked.

Since electrical heating and sample handling cause changes in the TiO$_2$ film and the intrinsic structure may change distinctly if several measurements and sample handlings are performed, only one round of TET measurement is conducted for each sample by feeding continuous periodic step DC signals, and repeated similar voltage profiles are recorded. One typical profile with both rising stage and steady state is extracted from the data for further analysis. In data analysis, different thermal diffusivity values of the sample are used to calculate the theoretical temperature rise. The one giving the best fit of the experimental data is taken as the property of the sample. The normalized curve generated by the least square fitting method is displayed in Fig. 5b for the sample presented in Fig. 5a. Based on this methodology, the thermal diffusivity of the sample is found to be 3.20×10^{-6} m^2 s^{-1}, which is close to the literature bulk thermal diffusivity of 3.17×10^{-6} m^2 s^{-1} for TiO$_2$ [43], while the discrepancy stems from both the interior fiber-like structure, which may affect the thermal transport and the dimension measurement uncertainty. As well as the experimental and theoretical curves, two more curves are also shown in Fig. 5b to present how the fitting uncertainty is determined by altering the thermal diffusivity to be slightly different from the true value and examining how distinct the deviation is. The altered

Table 1
Details of experimental parameters and results for a selected TiO$_2$ thin film characterized using the TET technique.

Length (mm)	2.63 ± 0.05
Width (mm)	0.56 ± 0.02
Thickness (μm)	57.0 ± 5.7
Resistance (Ω)	44.5 ± 0.2
DC current (mA)	4.00 ± 0.02
Effective density (kg m^{-3})	53.1 ± 6.9
Measured thermal diffusivity ($\times 10^{-6}$ m^2 s^{-1})	3.20 ± 0.26
Real thermal diffusivity ($\times 10^{-6}$ m^2 s^{-1})	2.97 ± 0.24
Effective thermal conductivity (W m^{-1} K^{-1})	0.13 ± 0.014
Real thermal conductivity (W m^{-1} K^{-1})	0.12 ± 0.013

(a)

(b)
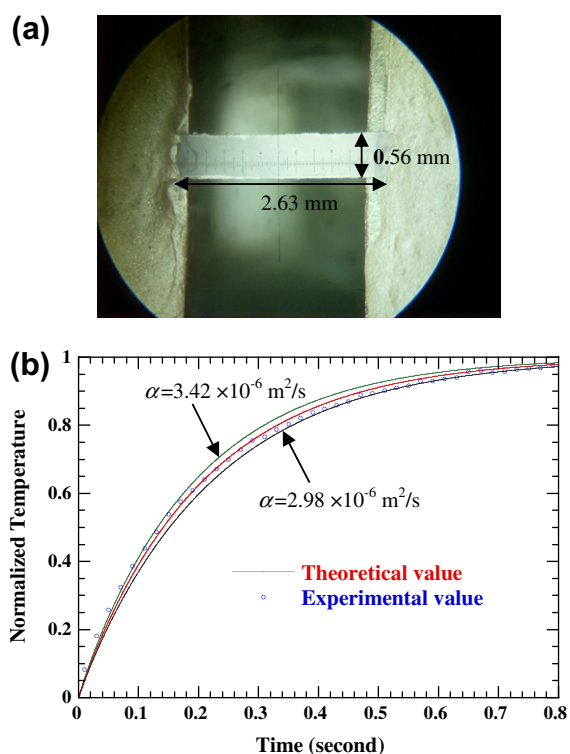
Fig. 5. (a) Microscopic image of the selected sample listed in Table 1, and (b) comparison between normalized temperature rise vs time between theoretical and experimental data for the sample shown in (a), while another two profiles considering fitting uncertainty are also plotted for comparison.

thermal diffusivities are 3.42 and 2.98×10^{-6} m^2 s^{-1}, respectively, suggesting that the uncertainty from data fitting is ~7%. Another important factor that influences the accuracy of the results is the length measurement. According to Eqs. (3) and (4), the accuracy of the normalized temperature and voltage is sensitive to the L^2 term, which doubles the uncertainty introduced by length measurement. What is attained by this methodology is not the real thermal diffusivity of the film. As discussed in the previous section, the TiO$_2$ was coated with a thin Au film in order to conduct the fed current. The thermal diffusivity obtained by the TET method has the effect introduced by Au coating, and this effect can be ruled out using the concept of thermal conductance, as indicated in Eq. (5), with known specific heat and density of the film.

The specific heat is mostly treated as a constant and does not change with temperature. However, in this study, the precise relationship between temperature and specific heat is required to suppress the uncertainty. Smith et al. [44] gave the detailed standard molar specific heat for anatase TiO$_2$ at different temperatures. The data are fitted with a polynomial curve for ease of future calculations, as presented in Fig. 6. Another critical issue in determining the real thermal diffusivity is the density. For bulk anatase TiO$_2$, the density is measured at 3.89×10^3 kg m^{-3} [43]. For loosely interconnected samples measured in this work, the density is estimated to be much less than
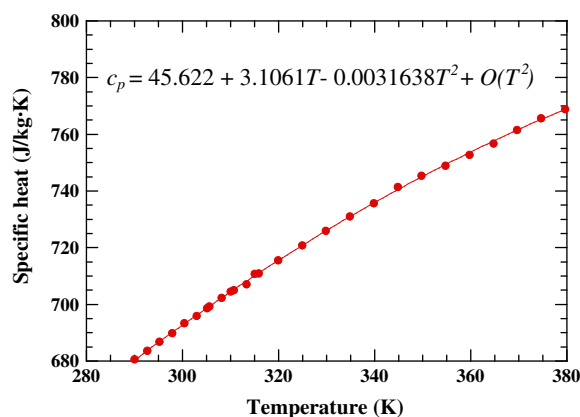
Fig. 6. Polynomial fitting of the relationship between specific heat and temperature for anatase TiO$_2$ [44].

3.89×10^3 kg m^{-3} because of the vacancies among the nanofibers that compose the film. Therefore, the correct estimation of the sample's density is important for further data processing. In order to estimate the density, the thermal conductivity of the film is required to be calculated in advance.

The thermal conductivity of the sample is obtained using the calibration of the temperature coefficient of resistance η as in the previous analysis. The heating power and temperature range are controlled to be moderate to make sure that the sample will not be overheated and that the unnecessary heat dissipation is negligible. A profile of the temperature coefficient of resistance is displayed in Fig. 7 for the sample summarized in Table 1. Because the Au coating significantly strengthens the electrical conduction of the sample, the calibration profile obtained presents a temperature–resistance property similar to a good conductor. A linear relationship is fitted to obtain the temperature coefficient of resistance, which is 2.4×10^{-2} Ω K^{-1} for this sample. The 95% confidence intervals for slope and intercept of the fitting equation are (0.02437, 0.02439) and (37.008 37.017), respectively. In addition, the square root of coefficient of determination r is 0.9976 (stated in the figure), which suggests that this regression model almost ideally fits the data. The uncertainty from resistance measurement is as small as 0.02%, and the error bars are added in this figure for the variation range of each reading. With a supplied DC current of 4 mA in the TET experiment, the recorded resistance change of the sample at a steady state is 0.89 Ω, which further helps to determine that the total temperature change is ~36.5 K. According to the expression of thermal conductivity, with known dimensional parameters and power, it is calculated to be 0.13 W m^{-1} K^{-1}, as listed in Table 1, and the effective density is also derived as $k_{eff}/(\alpha_e \cdot c_p)$. With this expression, the density is calculated to be 53.11 kg m^{-3}, which is almost two orders of magnitude lower than the literature value of ~3.89×10^3 kg m^{-3}; the modification based on Eq. (5) is available to exclude the influence of Au coating. The modified real thermal diffusivity of the film is
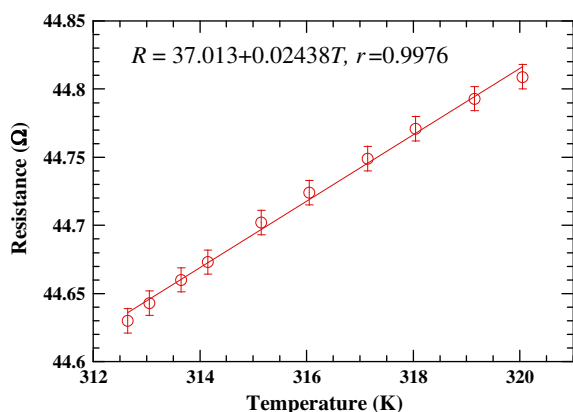
Fig. 7. Linear fitting curve of temperature coefficient of resistance for the sample listed in Table 1.

2.94×10^{-6} m^2 s^{-1}, which is ~8% smaller than the effective thermal diffusivity. This indicates that the Au coating has a negligible impact on the entire measurement.

In addition, the effective thermal conductivity obtained by the temperature rises until the steady state includes the impact introduced by Au coating. This impact can be ruled out following similar methodology to modify the effective thermal diffusivity. The real thermal conductivity of the sample is obtained using Eq. (6), and the value is also listed in Table 1.

$$k = k_{eff} - \frac{L_{Lorenz} TL}{RA_w} \qquad (6)$$

From Table 1, the thermal conductivity of the thin film is only 0.12 W m^{-1} K^{-1}, more than one order of magnitude lower than the bulk thermal conductivity of 8.5 W m^{-1} K^{-1} [43]. This is because the loose structure and existing vacancies greatly reduce the heat conduction inside the film, and also the existence of boundaries oriented perpendicular to the heat flow direction impacts the effective heat conduction. Regarding some substances that may exist in the wire interior, most water content is removed by annealing up to 500 °C. Although the annealed sample absorbs a certain amount of water and gas contents to the surface, owing to the short time that it is exposed to air, very limited numbers of H$_2$O, O$_2$ and N$_2$ molecules are absorbed at the surface of the TiO$_2$ nanofibers. No distinct impact is caused, because sparse molecules affect the lattice vibration transport procedure very little and leave the interior structures, vacancies and dislocations intact during the whole experiment.

3.2. Thermo-physical properties of samples with different dimensions

Samples of various dimensions are measured in this work to explore the relationship between their physical parameters and thermo-physical properties. Detailed information of all the samples is listed in Table 2, along with the modified thermo-physical properties and effective density. The thermal conductivity and diffusivity in Table 2 are the values after subtracting the effect of the Au coating. Depending on the duration time and imposed voltage of the electrospinning process, the film thickness varies from 50 to 80 µm, and all feature a loosely interconnected structure. As in the previous analysis, because of the nature of the interior loose structure, the thickness of a sample cannot be measured precisely, and only approximate values are employed in the calculation, which has introduced ~10% uncertainty into the calculation. Calculated thermal conductivities are one order of magnitude lower than bulk material, 8.5 W m^{-1} K^{-1} [43], which proves that the vacant structure within the sample has substantially attenuated the transport of phonon and consequently reduced the thermal conductivity. Based on the expression for thermal conductivity, if the sample is given ~10% measurement error, the uncertainty introduced to the thermal conductivity would not bring significant influence to the calculated results. Also listed in Table 2 are the measured results of a sample before annealing. The as-spun sample comprises both amorphous TiO$_2$ and PVP polymer content, while annealing at 500 °C selectively removes the PVP content and converts the amorphous TiO$_2$ structure into anatase polymorph. The measured thermal diffusivity of the unannealed sample is one order of magnitude higher than the results of the annealed samples, which shows that the vacancies in between the nanofibers could weaken the heat

Table 2
Experimental data and calculated results for all samples.

	Length (mm)	Width (mm)	Thickness (µm)	DC current (mA)	ΔR/ΔT (Ω K^{-1})	Effective density (kg m^{-3})	Thermal diffusivity (10^{-6} m^2 s^{-1})	Thermal conductivity (W m^{-1} K^{-1})
Unannealed sample	2.28 ± 0.05	1.14 ± 0.03	30.0 ± 3.0	2.00 ± 0.01			37.3 ± 3.0	
Sample 1	1.31 ± 0.03	0.79 ± 0.02	55.0 ± 5.5	4.00 ± 0.02	0.014	25.8 ± 3.4	3.07 ± 0.25	0.06 ± 0.007
Sample 2	1.07 ± 0.02	0.55 ± 0.02	67.5 ± 6.8	4.00 ± 0.02	0.044	38.4 ± 5.0	3.52 ± 0.28	0.10 ± 0.011
Sample 3	2.63 ± 0.05	0.56 ± 0.02	57.0 ± 5.7	4.00 ± 0.02	0.024	53.1 ± 6.9	2.97 ± 0.24	0.12 ± 0.013
Sample 4	2.45 ± 0.05	0.98 ± 0.03	82.5 ± 8.3	6.00 ± 0.03	0.038	109 ± 14.2	2.72 ± 0.22	0.21 ± 0.023
Sample 5	1.39 ± 0.03	0.65 ± 0.02	60.5 ± 6.1	6.00 ± 0.03	0.034	160 ± 20.8	2.14 ± 0.17	0.24 ± 0.026
Sample 6	1.85 ± 0.04	0.95 ± 0.03	59.5 ± 6.0	6.00 ± 0.03	0.031	217 ± 28.2	1.93 ± 0.15	0.30 ± 0.03
Sample 7	1.36 ± 0.03	0.53 ± 0.02	63.5 ± 6.3	4.00 ± 0.02	0.070	373 ± 48.5	1.36 ± 0.11	0.36 ± 0.04
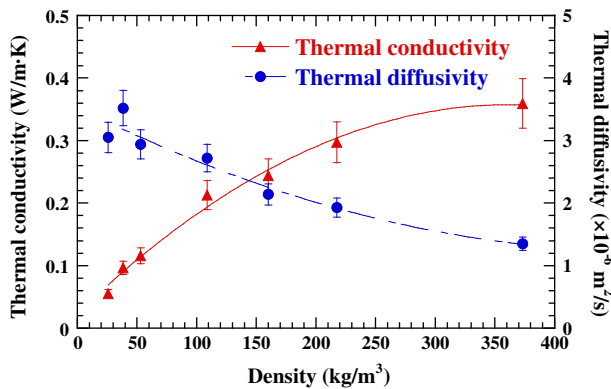
Fig. 8. Thermal conductivity and thermal diffusivity of TiO$_2$ thin films vs the density for the samples listed in Table 2; the curves are used to help the reader clearly view the data trend.

Fig. 9. Schematic of an infinitesimal volume for deriving intrinsic thermal conductivity of TiO$_2$ nanofibers.

transfer process because the annealing removes the PVP polymer and creates more vacancies.

Fig. 8 illustrates the variation in thermal conductivity and thermal diffusivity vs effective density, which is calculated based on measured thermal diffusivity and thermal conductivity. The effective density changes a lot from sample to sample, which means that it mainly depends on the preparation procedure. While the effective density ranges from ~25 kg m^{-3} to 370 kg m^{-3}, the thermal conductivity also varies substantially and displays a relatively ascending profile with density increase, which is consistent with Maekawa et al.'s conclusion [5]. This can be interpreted as when density increases, more nanofibers and fewer vacancies appear in the film and, therefore, heat conduction is enhanced. Certain discrepancies are observed in this figure and may be attributed to the impurity and defects in the crystal structure. First, the existence of the defects impairs phonon transport and consequently induces lower thermal conductivity. Second, dimensional uncertainty introduced by measurement would also bring slight uncertainty to the calculated thermal conductivity.

The profile of thermal diffusivity changing with density is also displayed in Fig. 8, and a profile contrary to the thermal conductivity is observed for the measured samples. With an increase in density, the thermal diffusivity decreases from 3.05×10^{-6} m^2 s^{-1} to 1.35×10^{-6} m^2 s^{-1}. Although the ability of the sample to conduct heat is enhanced with a higher density, the more condensed structure simultaneously reinforces the capability to store heat. This comprehensive effect weakens the thermal diffusivity, because the capability to store heat is augmented more than the ability to conduct heat. Deviation is also observed, and it follows the explanation similar to the thermal conductivity. These samples may have impurities and defects inside the crystal structure that cause variations in the capability of conducting heat. In addition, for each value in Fig. 8, error bars are added for measurement uncertainties, and detailed analysis to derive the uncertainties is given in Section 3.4.
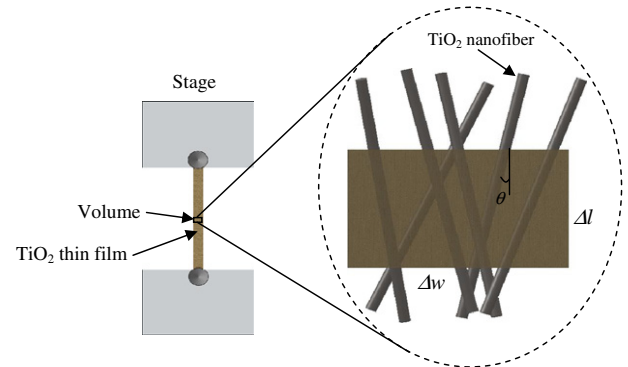
3.3. Intrinsic thermal conductivity of TiO$_2$ nanofibers

The calculated thermal conductivity is the overall (effective) value of the film. From Table 2 it can be observed that the values are significantly lower than the typical bulk thermal conductivity of 8.5 W m^{-1} K^{-1} [43]. The interpretation for this significant difference is that for the measured samples, the loose and disordered internal crystalline structure reduced the thermal energy transfer between molecules by phonons to a significant degree. When the effective thermal conductivity of the whole film is obtained, deriving the intrinsic thermal conductivity of the discrete TiO$_2$ nanofibers becomes feasible, and a physical model is designed to fulfill this purpose. The schematic of the model is displayed in Fig. 9. An infinitesimal volume is presumed to accommodate a certain number of TiO$_2$ nanofibers, the total number of which in unit cross-sectional area is n, and the average cross-sectional area is A_f. Assumptions are made that the presumed volume is small enough to comprise minimal interconnection of nanofibers, and the heat transfer within each nanofiber does not influence the heat transfer in its neighbors. The length and width of this infinitesimal volume are Δl and Δw, respectively. This small volume has a unit length in the direction normal to the paper.

The thermal conductance of the whole volume is attributed to the contribution of every single TiO$_2$ nanofiber. Therefore, considering an arbitrary alignment angle θ, the thermal conductance along the vertical direction for a fiber is

$$\frac{2}{\pi} \int_0^{\pi/2} \frac{k_f A_f}{\Delta l / \cos\theta} d\theta \cdot n \cdot \Delta w = \frac{k \cdot \Delta w}{\Delta l} \tag{7}$$

Then the thermal conductivity of a single nanofiber is $k_f = (\pi/2) \cdot k / (A_f \cdot n)$. The effective length of a single nanofiber is determined as $l_{eff} = (2/\pi) \int_0^{\pi/2} \frac{\Delta l}{\sin\theta + \cos\theta} d\theta = 0.793 \Delta l$. Similarly, the total mass of this volume is estimated as the sum of the mass of each nanofiber as $l_{eff} \cdot A_f \cdot \rho_f \cdot n \cdot \Delta w \cdot 1 = \Delta l \cdot \Delta w \cdot 1 \cdot \rho_{eff}$. Then the total number of TiO$_2$ nanofibers n is calculated as $\rho_{eff}/(0.793 A_f \rho_f)$. The intrinsic thermal conductivity of TiO$_2$ nanofibers is then calculated as

$$k_f = \frac{\pi}{2} \frac{0.793 k \rho_f}{\rho_{eff}} = 1.246 \rho_f \alpha c_p \tag{8}$$

From Eq. (8), the intrinsic thermal conductivity of TiO_2 nanofibers is related to bulk density, thermal diffusivity and specific heat. Calculated results based on Eq. (8) for all samples are listed in Table 3. It is observed that the intrinsic thermal conductivities are an order of magnitude higher than the measured value of the thin films and of the same order of magnitude as the reported bulk thermal conductivity, $8.5\,W\,m^{-1}\,K^{-1}$ [43], where discrepancies are observed. Such discrepancies could come from the physical model used here. Based on the AFM images, the nanofibers contain both straight and curved features. Therefore, the straight shape of nanofibers is an idealized scenario. In addition, the target volume is assumed to contain minimal interconnections for simplicity. However, in practical composition, the structure shows distinct entangled characteristics, and the interaction between nanofibers cannot be ignored. Second, the uncertainty coming from the estimation of thermal diffusivity also impacts the results according to Eq. (8). The thickness of each film could have a large uncertainty in measurement because of the interior loose structure of the film. Inside the films, a large number of vacancies exist, which also brings uncertainty into the measurement and calculation.

The mean free path of phonons in the sample is consequently calculated based on the calculated intrinsic thermal conductivity to estimate the effect of nanofiber thickness and length. Thermal conductivity is known related to heat capacity per volume C, particle group velocity (phonons) v and mean free path l, as $k_f = 1/3 C v l$. The typical value of heat capacity C for anatase TiO_2 is $2.76 \times 106\,J\,m^{-3}\,K^{-1}$. The sound velocity of anatase crystal is applied here as the group velocity of phonons and a mean value of $4181\,m\,s^{-1}$ [45] which is employed in the calculation. The calculated phonon mean free path for each sample is listed in Table 3, and the results fall within the range 1–3 nm. According to the AFM images, the length and thickness of nanofibers are substantially greater than the phonon mean free path. Therefore, the scale of the sample boundary has no strong influence on the phonon transport, and the major restriction on the heat conduction comes from the crystalline structural defect.

Table 3
Intrinsic thermal conductivity of discrete TiO_2 nanofibers and derived mean free path of all samples.

	Real thermal conductivity (W m^{-1} K^{-1})	Intrinsic thermal conductivity of nanofibers (W m^{-1} K^{-1})	Mean free path of phonons (nm)
Sample 1	0.06 ± 0.007	10.4 ± 0.83	2.73
Sample 2	0.10 ± 0.011	12.2 ± 0.98	3.15
Sample 3	0.12 ± 0.013	10.6 ± 0.85	2.93
Sample 4	0.21 ± 0.023	9.48 ± 0.76	2.43
Sample 5	0.24 ± 0.026	7.40 ± 0.59	1.92
Sample 6	0.30 ± 0.03	6.63 ± 0.53	1.72
Sample 7	0.36 ± 0.04	4.67 ± 0.37	1.21

The work reported in this paper focuses on the study of thermo-physical properties of films composed of TiO_2 nanowires, then the evaluation of the intrinsic thermal conductivity of individual TiO_2 nanowires. It will be of great interest if the thermo-physical properties of individual TiO_2 nanowires can be measured directly using the TET technique. Future work will focus on fabricating single TiO_2 nanowires aligned between two electrodes using electrical field alignment and characterizing their thermo-physical properties.

3.4. Uncertainty analysis

From the aforementioned experimental procedure, the sources of uncertainty in this work may be divided into two major aspects: dimension measurement and data fitting. They impose different effects on the thermo-physical properties, and the details are discussed below.

The uncertainty of thermal diffusivity is introduced by both length measurement and data fitting. From Eqs. (3) and (4), the L^2 term in the exponent contributes to the uncertainty from measuring the length of the sample. This uncertainty is small, and it is estimated to be within 2%. Therefore, uncertainty from length measurement is ~4% in total for L^2. Uncertainty from data fitting is determined by altering the thermal diffusivity to examine how large the deviation is between the fitted curve from the altered parameters and the curve from the true value. The fitting uncertainty is found at ~7%, as discussed before. Therefore, the total uncertainty for thermal diffusivity is ~8%, based on error propagation theory.

From Guo et al.'s work [38], the thermal conductivity is expressed as $k = q_0 L/(12 A \Delta T)$, which suggests that the source of uncertainty for thermal conductivity consists of three parts: the electrical heating power q_0, the temperature difference ΔT, and dimensional parameters (length L and cross-sectional area A). The electrical heating power is generated by a constant current source, and therefore q_0 includes a negligible error of ~1%. For temperature difference, it is read directly from the experimental U–t profile, and the uncertainty is estimated to be <0.5%. The major source of uncertainty for thermal conductivity is the dimension measurement. For length measurement, as analyzed before, the uncertainty is ~2%. For width, also directly measured from the sample, the uncertainty is estimated to be 3%. The thickness has the largest measurement of uncertainty of the above discussions at ~10%. Considering all sources of uncertainty, the uncertainty of thermal conductivity is ~11%.

The density is derived from thermal conductivity, thermal diffusivity and specific heat, based on the expression $\rho = k/(\alpha c_p)$. The uncertainties for thermal conductivity and thermal diffusivity are already determined as 11% and 8%, respectively. The data for specific heat are extracted from Smith et al.'s work [44]. From uncertainty propagation, the total uncertainty for density is estimated to be 13%. The measured thermal diffusivity and thermal

conductivity still include the impact from gold coatings. Therefore, uncertainty rises when modification is conducted based on Eqs. (5) and (6). The modification terms to exclude the impact of gold coatings in both equations are <10% of the effective value. After accounting for uncertainty, the error generated by the modification terms is almost negligible compared with the error introduced by the effective terms. The uncertainty from effective terms yields actual uncertainty of 8% for real thermal diffusivity and 11% for real thermal conductivity. Based on Eq. (8), intrinsic thermal conductivity is determined using bulk density of TiO_2, thermal diffusivity and specific heat. The uncertainty of intrinsic thermal conductivity is linearly dependent on thermal diffusivity and is estimated to be 8%.

From the above analysis, it is concluded that the uncertainties of major parameters in this experiment are controlled within acceptable ranges considering the samples' differences and varying experimental conditions. The uncertainties in the results are listed in Tables 1–3.

4. Conclusion

In this paper, TiO_2 thin films with thickness ∼60 μm were fabricated using an electrospinning technique, and interior interconnected TiO_2 nanofibers were confirmed by AFM images. The Raman spectrum indicated anatase polymorph of TiO_2 after annealing at 500 °C. The TET technique was adopted to provide a full spectrum measurement of the film thermal diffusivity, density and thermal conductivity. The effective thermal conductivity obtained ranges from 0.06 to 0.36 W m^{-1} K^{-1} while the effective density changes from 25.8 to 373 kg m^{-3}, significantly lower than the reported bulk property value due to the disordered and loose crystalline-structured nature of the sample films. This means that bulk property values may not be appropriate in the design of thin optical films. With the density increase, the thermal conductivity presented an ascending profile showing that the thermal conductivity of thin films is strongly influenced by the density. A physical model was developed to estimate the intrinsic thermal conductivity of TiO_2 nanofibers based on the measured thermal properties of the thin films. The calculated intrinsic thermal conductivity (4.67–12.2 W m^{-1} K^{-1}) of TiO_2 nanofibers varies within a range one order of magnitude higher than that of the thin film, and is acceptably comparable with the value of bulk material of 8.5 W m^{-1} K^{-1}, considering the uncertainty introduced into the model and experiment. A calculation of mean free path based on the intrinsic thermal conductivity of TiO_2 nanofibers demonstrates that the nanofiber size has a negligible impact on the phonon transport, and the major restriction on the heat transfer originated from the crystalline structure defect.

Acknowledgements

References

[1] Jung KY, Park SB. J Photochem Photobiol A 1999;127:117.
[2] Jung KY, Park SB. Appl Catal B – Environ 2000;25:249.
[3] De Farias RF, Guedes E, Silva CC, Restivo TAG. J Serb Chem Soc 2005;70(4):675.
[4] Halary E, Benvenuti G, Wagner F, Hoffmann P. Appl Surf Sci 2000;154–155:146.
[5] Maekawa T, Kurosaki K, Tanaka T, Yamanaka S. Surf Coat Technol 2008;202:3067.
[6] Wang KH, Hsieh YH, Lin TT, Chang CY. React Kinet Catal Lett 2008;95:39.
[7] Li D, Wang YL, Xia YN. Nano Lett 2003;3:1167.
[8] Subbiah T, Bhat GS, Tock RW, Parameswaran S, Ramkumar SS. J Appl Polym Sci 2005;96:557.
[9] Son WK, Cho D, Park WH. Nanotechnology 2006;17:439.
[10] Li D, Xia YN. Nano Lett 2003;3:555.
[11] Tekmen C, Suslu A, Cocen U. Mater Lett 2008;62:4470.
[12] Zhu R, Jiang CY, Liu XZ, Liu B, Kumar A, Ramakrishna S. Appl Phys Lett 2008;93:013102.
[13] Rinaldi M, Ruggieri F, Lozzi L, Santucci S. J Vac Sci Technol B 2009;27(4):1829.
[14] Li YL, Ishigaki T. J Phys Chem B 2004;108:15536.
[15] Wang WZ, Varghese OK, Paulose M, Grimes CA, Wang QL, Dickey EC. J Mater Res 2004;19:417.
[16] Poudel B, Wang WZ, Dames C, Huang JY, Kunwar S, Wang DZ, et al. Nanotechnology 2005;16:1935.
[17] Xu CK, Zhan YJ, Hong KQ, Wang GH. Solid State Commun 2003;126:545.
[18] Zhang DY, Qi LM. Chem Commun 2005:2735.
[19] Štengl V, Bakardjieva S, Murafa N, Večerníková E, Šubrt J, Balek V. J Nanopart Res 2007;9:455.
[20] Boercker JE, Enache-Pommer E, Aydil ES. Nanotechnology 2008;19:095604.
[21] Adachi M, Murata Y, Takao J, Jiu JT, Sakamoto M, Wang FM. J Am Chem Soc 2004;126:14943.
[22] Huber B, Gnaser H, Ziegler C. Anal Bioanal Chem 2003;375:917.
[23] Choi Y, Yamamoto S, Umebayashi T, Yoshikawa M. Solid State Ionics 2004;172:105.
[24] Huber B, Gnaser H, Ziegler C. Surf Sci 2004;566–568:419.
[25] Obida MZ, Afify HH, Abou-Helal MO, Zaid HAH. Egypt J Solids 2005;28:35.
[26] Shen QH, Yang H, Gao JW, Yang JG. Mater Lett 2007;61:4160.
[27] Zhou XS, Li LJ, Lin YH, Nan CW. J Electroceram 2008;21:795.
[28] Agarwala S, Ho GW. Mater Lett 2009;63:1624.
[29] Wu YH, Long MC, Cai WM, Dai SD, Chen C, Wu DY, et al. Nanotechnology 2009;20:185703.
[30] Gu GR, He Z, Tao YC, Li YA, Li JJ, Yin H, et al. Vacuum 2003;70:17.
[31] Zhang XR, Lin S, He J, Li GH, Zhang LD. Rev Prog Quant Nondestructive Eval 2003;22:1292.
[32] Lambropoulos JC, Jolly MR, Amsden CA, Gilman SE, Sinicropi MJ, Diakomihalis D, et al. J Appl Phys 1989;66:4230.
[33] Wu ZL, Reichling M, Hu XQ, Balasubramanian K, Guenther KH. Appl Opt 1993;32:5660.
[34] Cahill DG, Allen TH. Appl Phys Lett 1994;65(3):309.
[35] Lee SM, Cahill DG, Allen TH. Phys Rev B 1995;52:253.
[36] Mun J, Kim SW, Kato R, Hatta I, Lee SH, Kang KH. Thermochim Acta 2007;455:55.
[37] Martan J, Hervé O, Lang V. J Appl Phys 2007;102:064903.
[38] Guo JQ, Wang XW, Wang T. J Appl Phys 2007;101:063537.
[39] Feng B, Ma WG, Li ZX, Zhang X. Rev Sci Instrum 2009;80:064901.
[40] Guo LY, Wang J, Lin ZQ, Gacek S, Wang XW. J Appl Phys 2009;106:123526.

[41] Ohsaka T, Izumi F, Fujiki Y. J Raman Spectrosc 1978;7:321.

[42] Yoshitake H, Abe D. Microporous Mesoporous Mater 2009;119:267.

[43] Anthony JW, Bideaux RA, Bladh KW, Nichols MC. Handbook of mineralogy volume III halides, hydroxides, oxides. Arizona: Mineral Data Publishing; 1997.

[44] Smith SJ, Stevens R, Liu SF, Li GS, Navrotsky A, Boerio-Goates J, et al. Am Mineral 2009;94:236.

[45] Shojaee E, Mohammadizadeh MR. J Phys: Condens Matter 2010;22:015401.